

ARTICLE OPEN

Long-ranged Cu-based order with $d_{x^2-y^2}$ orbital character at a YBa₂Cu₃O₇/manganite interface

Roxana Gaina^{1,2,5} , Christopher W. Nicholson^{1,5} , Maxime RUMO¹ , Subhrangsu Sarkar¹, Jarji Khmaladze¹, Eugenio Paris³, Yi Tseng³, Wenliang Zhang³, Teguh C. Asmara³ , Daniel McNally³, Cinthia Piamonteze³, Eugen Weschke⁴, Thorsten Schmitt³ , Claude Monney¹  and Christian Bernhard¹ 

The interplay of nearly degenerate orders in quantum materials can lead to a myriad of emergent phases. A prominent case is that of the high- T_c cuprates for which the relationship between superconductivity and a short-ranged, incommensurate charge density wave in the CuO₂ planes involving the $d_{x^2-y^2}$ orbitals (Cu-CDW) is a subject of great current interest. Strong modifications of the strength and coherence of this Cu-CDW have been achieved by applying large magnetic fields, uniaxial pressure, or via the interfacial coupling in cuprate/manganite multilayers. However, such modifications do not alter the dominant orbital character. Here we investigate cuprate/manganite multilayers with resonant inelastic X-ray scattering (RIXS) and show that a new kind of Cu-based density wave order can be induced that has not been previously observed in the cuprates. This order has an unusually small in-plane wave vector in the range of $Q_{||} < 0.1$ reciprocal lattice units (r.l.u.), a large correlation length of about 40 nm, and a predominant d_{z^2} orbital character, instead of the typical $d_{x^2-y^2}$ one. Its appearance is determined by the hole doping of the manganite which is a key parameter controlling the interfacial charge transfer and orbital reconstruction. We anticipate that the observation of a previously unknown type of density wave order at the YBCO interface will allow for fresh perspectives on the enigmatic relation between superconductivity and charge order (CO) in the cuprates.

npj Quantum Materials (2021) 6:12; <https://doi.org/10.1038/s41535-021-00311-y>

INTRODUCTION

The complex phase diagram of the cuprate high- T_c superconductors is a prime example of the varied properties of strongly correlated quantum materials that arise from competing orders and nearly degenerate ground states¹. Besides the enduring puzzle of the superconducting pairing mechanism, the exact nature of the normal state in these materials remains elusive. In particular, in the underdoped regime where a so-called pseudogap depletes the low-energy electron states already well above T_c ²⁻⁴, various spin and/or charge orders have been found to coexist with superconductivity. Intense studies have been carried out on the remnants of antiferromagnetic (AF) correlations in the strongly underdoped regime^{5,6} and on the so-called stripe order with coupled spin and charge modulations in La_{1.875}Ba_{0.125}CuO₄^{7,8}. More recently, the focus has shifted to an incommensurate Cu-CDW order that was first observed in underdoped YBa₂Cu₃O_{7- δ} (YBCO)^{9,10}, and, meanwhile, also in several other compounds. In bulk samples at ambient conditions this static Cu-CDW, with a wave vector of $Q_{||} \approx 0.25$ – 0.3 reciprocal lattice units (r.l.u.) and $d_{x^2-y^2}$ orbital character, is relatively weak and short-ranged. Its relationship with superconductivity remains controversial, with the proposed scenarios ranging from simple competition¹¹, over intertwined orders such as the enigmatic pair-density wave state^{12,13}, to a superconducting pairing mechanism that is mediated by CDW-fluctuations¹⁴⁻¹⁶. It is still debated whether the short-range CDW correlations are driven by Fermi-surface nesting¹⁷, or rather by a tendency towards charge segregation provoked by strong electronic correlations¹⁶. However, the recent observation of a re-entrant Cu-CDW with a small

wave vector of $Q_{||} = 0.15$ r.l.u. in strongly overdoped Bi-2201 is difficult to reconcile with a pure nesting scenario¹⁶.

Various successful attempts have been undertaken to enhance and modify the Cu-CDW in order to further explore its origin and relationship with superconductivity. In underdoped YBCO, the strength and the correlation length of the Cu-CDW with $Q_{||} \approx 0.3$ r.l.u. have been strongly enhanced by applying large magnetic fields that suppress superconductivity^{18,19} or uniaxial pressure along the a -axis, which enhances the orthorhombicity, but suppresses SC only partially²⁰. In both cases, there appears to be a strong competition between SC and the long-range CDW. A strong enhancement of the Cu-CDW with $Q_{||} \approx 0.3$ r.l.u. has also been achieved in YBCO/manganite multilayers for which the competition with superconductivity appears to be weak²¹. Moreover, for YBCO/Nd_{1-x}(Ca_{1-y}Sr_y)_xMnO₃ (YBCO/NCSMO) multilayers with $x = 0.35$, it has been demonstrated that the magnitude of the Cu-CDW can be strongly modified via the tolerance factor (or the Sr content) NCSMO, which controls its intrinsic charge and orbital (CO) order²².

The YBCO layers of the latter YBCO/NCSMO multilayers have anomalous superconducting properties. For multilayers for which the tolerance factor, t (or the Sr content, y) of the manganite is small enough to induce an insulating state with CE-type charge and orbital (Mn-CO) order, the YBCO layers exhibit a granular superconducting state which gives rise to an insulator-like upturn of the resistance below T_c , instead of the expected drop to zero resistance²²⁻²⁴. This unusual behavior occurs only in multilayers for which the thickness of the YBCO layer is below a critical value of $d^{\text{YBCO}} \leq 7$ – 8 nm and where the manganite layers display the

¹University of Fribourg, Department of Physics and Fribourg Center for Nanomaterials, Chemin du Musée 3, CH-1700 Fribourg, Switzerland. ²Laboratory for Neutron Scattering and Imaging, Paul Scherrer Institut, CH-5232 Villigen, PSI, Switzerland. ³Swiss Light Source, Photon Science Division, Paul Scherrer Institut, CH-5232 Villigen, PSI, Switzerland.

⁴Helmholtz-Zentrum Berlin für Materialien und Energie, BESSY II, D-12489 Berlin, Germany. ⁵These authors contributed equally: Roxana Gaina, Christopher W. Nicholson.

email: roxana.gaina@unifr.ch; christian.bernhard@unifr.ch

Mn-CO^{23,25}. Notably, a coherent SC response below T_c can be restored here by the application of a large magnetic field²⁵, which is known to weaken and suppress the Mn-CO of the manganite. This unusual kind of magnetic-field-induced transition from an insulating to a superconducting state is absent in corresponding $\text{Nd}_{1-x}(\text{Ca}_{1-y}\text{Sr}_y)_x\text{MnO}_3 / \text{YBa}_2\text{Cu}_3\text{O}_7 / \text{Nd}_{1-x}(\text{Ca}_{1-y}\text{Sr}_y)_x\text{MnO}_3$ (NYN) multilayers for which the manganite has a larger tolerance factor (Sr content, y) and thus an itinerant ferromagnetic instead of the Mn-CO ground state²⁴. These trends suggest that the granular superconducting state of the YBCO layers is induced by a proximity effect due to the coupling with the Mn-CO of the adjacent manganite layers. While the interfacial coupling mechanism remains to be established, it seems likely that the concomitant induced (or strongly enhanced) Cu-CDW order in the YBCO layer plays an important role in the formation of the granular superconducting state.

This calls for further studies of the relationship between the manganite and cuprate charge/orbital orders in these multilayers. In the following, we present a combined resonant inelastic and elastic X-ray spectroscopy (RIXS and REXS) and X-ray absorption spectroscopy (XAS) study at the Cu L_3 -edge of a NYN trilayer with $x=0.5$ and $y=0.25$. In this sample, the hole doping of the manganite has been adjusted to obtain a long-ranged Mn-CO

order, unlike the previously studied multilayers with $x=0.3-0.35$ for which the Mn-CO is strongly disordered^{24,25}. To our surprise we find that a new kind of Cu-based order is induced in the YBCO layer that has an unusually short wave vector in the range of $Q_{\parallel} \approx 0.09-0.096$ r.l.u., a large correlation length of about 40 nm, and a predominant d_{z^2} character, rather than the standard $d_{x^2-y^2}$ one. Moreover, we identify the hole doping of the manganite layers as a key parameter that determines not only its own charge/orbital and magnetic order, but also allows modification of the interfacial charge transfer and the occupation of the d_{z^2} orbitals in the interfacial CuO_2 planes. Our observations provide insights into the interfacial coupling between the Mn- and Cu-based charge and magnetic orders, and they suggest a new route to induce coupled quantum states in these cuprate/manganite multilayers.

RESULTS

Different Bragg peaks of elastic RIXS signal at $x=0.5$ and 0.35

Figure 1a shows a sketch of a NYN trilayer and the scattering geometry of the RIXS setup. The scattering angle between the incident (\mathbf{k}_{in}) and scattered (\mathbf{k}_{out}) X-ray beams ($\Psi = 130^\circ$), and the resulting magnitude of the scattering vector $\mathbf{Q} = \mathbf{k}_{\text{in}} - \mathbf{k}_{\text{out}}$ are kept fixed during the experiment. The in-plane component Q_{\parallel} is varied

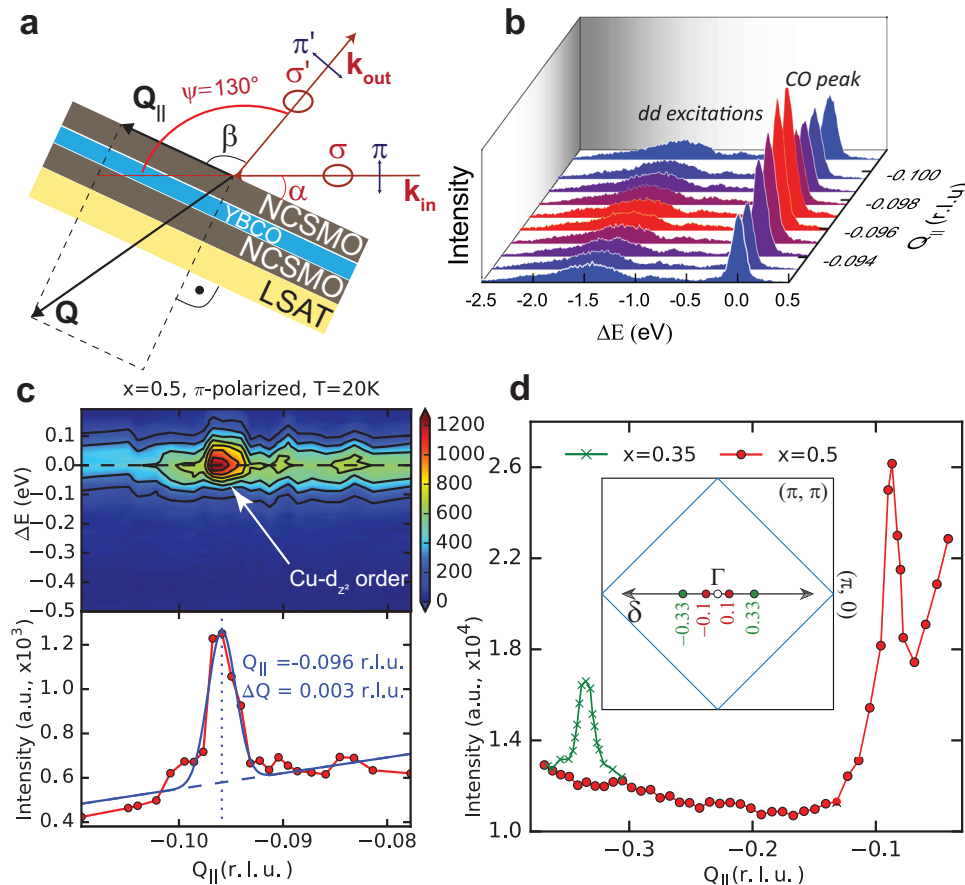


Fig. 1 Overview of the incommensurate Cu density wave orders in NYN trilayers obtained with RIXS. **a** Schematic of the RIXS experiment at the Cu L_3 -edge with X-rays with linear σ - and π -polarization. The scattering angle between incoming and outgoing beams is $\Psi = 130^\circ$. The angle δ , which gives the projection of transferred momentum along the surface direction, is defined as zero when the angles α and β are equal (specular reflection), i.e., $\delta \Psi / 2 - \alpha$. Therefore, grazing incidence corresponds to $\delta > 0$, while grazing exit corresponds to $\delta < 0$. **b** Observed RIXS spectra for different Q_{\parallel} at the Cu L_3 -edge for the trilayer with $x=0.5$ showing the elastic peak ($\Delta E = 0$) enhancement due to the CO and the inelastic signals ($\Delta E < 0$), at an incidence energy of 930.4 eV. **c** Evolution of the elastic peak intensity ($\Delta E = 0$) in π -polarization as a function of Q_{\parallel} , showing a pronounced Bragg peak at $Q_{\parallel} \approx 0.096$ r.l.u. due to a Cu-based order. **d** Wide-range Q_{\parallel} -scan showing that the ordinary Cu-CDW Bragg peak around $Q_{\parallel} \approx 0.33$ r.l.u. is absent for the trilayer with $x=0.5$. Shown for comparison are RIXS data of a trilayer with $x=0.35$ for which this latter Bragg peak is present and enhanced with respect to bulk YBCO (adapted from ref. ²²). The inset shows a schematic of the Brillouin zone and the positions of the two charge order peaks, which appear symmetrically about the Γ -point along the $(\pi, 0)$ direction.

here by rotating the sample, and is zero at specular reflection, when the angles α and β are equal (see Fig. 1a). The corresponding variation of the out-of-plane component Q_{\perp} is not considered in the following, since the Cu-based order is expected to be quasi-two-dimensional. Typical RIXS intensity spectra of the outgoing scattered photons as a function of their energy loss (ΔE) are displayed in Fig. 1b for different in-plane momentum transfer values. In the present case, the incident energy is resonant with the Cu L_3 -edge (i.e., resonant with a Cu $2p$ to $3d$ transition).

As a consequence, the elastic signal at $\Delta E = 0$ is very sensitive to the scattering from the Cu- $3d$ valence electrons and is used in the following to probe the Bragg peak of the charge/spin order of the Cu ions. The inelastic signal at $\Delta E < 0$ is not further discussed here, but contains rich information on phonons, magnons, and crystal field excitations between the Cu- $3d$ levels that will be presented elsewhere. As can be clearly observed in the raw data, a significant enhancement of the elastic peak is found within a particular range of Q_{\parallel} values, signifying the occurrence of a Bragg peak, and hence an underlying order.

The Q_{\parallel} dependence of the elastic signal of the NYN trilayer with $x = 0.5$ is analyzed in more detail in Fig. 1c, revealing a pronounced Bragg peak at an in-plane wave vector of $Q_{\parallel} \approx -0.096$ r.l.u. To obtain this curve, the RIXS spectra in Fig. 1b at different in-plane scattering vectors are obtained by rotating the sample with respect to the beam. The elastic part of the RIXS spectra is then summed to give the total elastically scattered intensity. Interestingly, the observed Bragg peak occurs at a much smaller wave vector than the one due to the ordinary Cu-CDW of YBCO, which is expected at $Q_{\parallel} \approx \pm 0.3$ r.l.u.¹⁰. The scan over a wider Q_{\parallel} -range in Fig. 1d reveals that no Bragg peak around $Q_{\parallel} \approx 0.3$ r.l.u. occurs for the $x = 0.5$ NYN trilayer. Also shown, for comparison, are the data of a NYN trilayer with $x = 0.35$ and $y = 0.2$ (green symbols) for which a pronounced Bragg peak is observed at $Q_{\parallel} \approx -0.33$ r.l.u.²². Correspondingly, from REXS data (see Supplementary Fig. 10, Supplementary Material), the $x = 0.35$ NYN trilayer shows no Bragg peak around $Q_{\parallel} \approx -0.096$ r.l.u. This observation of mutually exclusive Bragg peaks in the $x = 0.5$ and $x = 0.35$ NYN trilayers implies that the underlying orders are of different nature and are controlled by the hole doping of the manganite layers.

Comparably small ordering wave vectors as observed in the $x = 0.5$ NYN trilayer have only been reported for strongly overdoped Bi-2201 with $Q_{\parallel} \approx 0.15$ r.l.u.¹⁶, and for the spin component of the so-called stripe order of LBCO with $Q_{\parallel} \approx 0.125$ r.l.u.^{7,8}. The Bragg peak in the present case is also rather narrow with a half-width at half-maximum of $\Delta Q_{\parallel} \approx 0.003$ r.l.u. corresponding to a correlation length of $\xi = a(\pi\Delta Q_{\parallel})^{-1} \approx 39$ nm (using the in-plane lattice parameter $a = 3.87$ Å of the $\text{La}_{0.3}\text{Sr}_{0.7}\text{Al}_{0.65}\text{Ta}_{0.35}\text{O}_3$ (LSAT) substrate). This value is about an order of magnitude larger than for YBCO bulk or thin film samples, with the exception of the 3D-CDW that can be induced with high magnetic field^{18,19} and uniaxial pressure²⁰.

Polarization dependence of Bragg peak at $x = 0.5$

Further evidence of the distinct nature of the Cu-based order underlying the Bragg peak at $Q_{\parallel} \approx 0.096$ r.l.u. comes from measurements obtained at different polarizations, and from comparing the enhancement of the peak obtained on either side of Γ -point of the Brillouin zone (Fig. 1d, inset). The elastic scattering intensity measured in a RIXS experiment depends on geometric factors and the orbital character of the states involved in the scattering process. Particularly relevant are the electric field component of the X-ray beams with respect to the scattering plane (π or σ polarization), and the incident angle of the beam with respect to the sample surface (grazing incidence or grazing exit beam, see Fig. 1a). The latter of these defines the surface projection of the momentum transferred during the RIXS process, and hence the position in the Brillouin zone. The effect of these

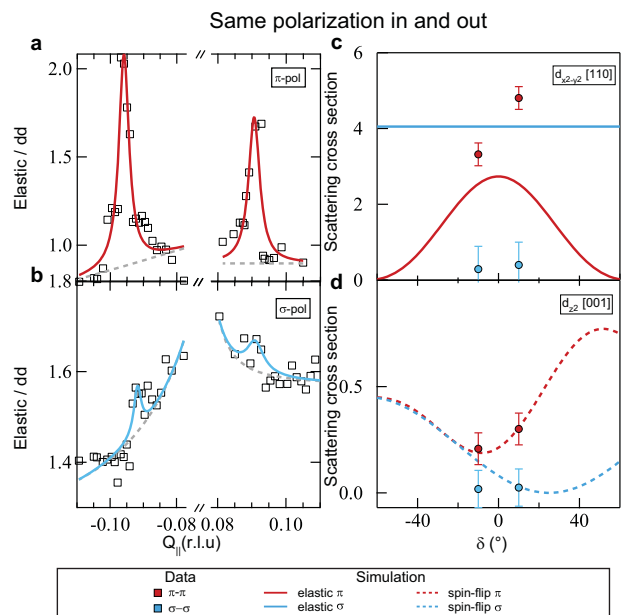


Fig. 2 Evidence for the d_{z^2} character of the Bragg peak of the $x = 0.5$ NYN-trilayer obtained at the Cu L_3 edge. **a, b** Normalized intensity of the elastic line from RIXS (open symbols) as a function of in-plane momentum transfer, Q_{\parallel} , of the incident X-rays for π - and σ -polarization, respectively. Solid lines are Lorentzian fits with a Gaussian background. The gray dashed lines highlight the background contribution. The increased peak intensity for the π -polarized beam are in direct contrast to previous observations of charge order involving $d_{x^2-y^2}$ orbitals. The combined uncertainty in Q_{\parallel} is ± 0.005 r.l.u. **c** Geometric scattering cross-section calculations (solid lines) for an elastic $d_{x^2-y^2}$ process as a function of angle δ . An angle of 0° corresponds to the Γ -point. The intensities of the Bragg peaks at the corresponding scattering conditions (obtained for each of the four cases in (a) and (b)) are shown as markers (30 \times magnified). The reversed polarization dependence compared with the calculations reveals the underlying orbital character cannot be $d_{x^2-y^2}$. **d** The same calculation as in (c) for a spin-flip scattering process involving d_{z^2} orbitals, and spin oriented along the [001] direction. The d_{z^2} orbital symmetry correctly captures the reversal of the measured π and σ cross-sections (markers, 2 \times magnified) compared with the $d_{x^2-y^2}$ case, highlighting the role of d_{z^2} orbitals in the observed order. Errors were calculated using standard deviations.

factors will clearly vary depending on the orbital symmetry involved in the scattering process, e.g., in-plane $d_{x^2-y^2}$ or out-of-plane d_{z^2} . Therefore, obtaining measurements under different geometries and comparing with scattering cross-section calculations for specific orbitals, allows the determination of the dominant orbital symmetry for a particular scattering process. Figure 2a, b shows the Q_{\parallel} scans at 930.4 eV for π and σ polarization in grazing incidence (incident angle > 0) and grazing exit (incident angle < 0) geometries. The overlaid fits of the Bragg peak are obtained using a Lorentzian line-shape and an exponential background; dashed gray lines show the background contribution. We observe that the Bragg peak enhancement is considerably larger for π -polarization than for σ -polarization for both grazing incidence and exit geometries. This corresponds to a complete reversal compared with previous reports of $d_{x^2-y^2}$ order^{10,16}, where σ -polarization shows the strongest signal. This suggests that the behavior underlying the newly observed Bragg peak corresponds to a different orbital symmetry than in previous observations. This finding is further highlighted in Fig. 2c, which compares the maximum Bragg peak intensities (symbols) obtained under the different scattering conditions presented in Fig. 2a, b with the corresponding calculated RIXS cross-sections as

a function of δ . By comparing the expectations of the RIXS cross-sections for a $d_{x^2-y^2}$ orbital under the same scattering conditions as in the experiment, see Fig. 2c, it is immediately clear that the observed geometric dependence cannot be explained by a dominant $d_{x^2-y^2}$ orbital character that is typically observed in the cuprates.

Instead, the enhancement of the Bragg peak intensity with out-of-plane light polarization indicates the participation of d_{z^2} orbitals. Indeed, we find a reasonable agreement with the calculated RIXS cross-sections for scattering into d_{z^2} states with a spin-flip process. The calculated curves for spin-flip processes with spins oriented along [001] are shown in Fig. 2d, and are again compared with the measured Bragg peak intensities. In particular, the spin-flip scattering involving d_{z^2} orbitals correctly predicts the observed reversal of cross-sections compared with the $d_{x^2-y^2}$ case in Fig. 2c. This therefore implies a dominant role of the out-of-plane d_{z^2} orbitals in the $Q_{\parallel} = 0.096$ r.l.u. order. In the supplementary materials (Supplementary Note 4 and Supplementary Fig. 3), we present comparisons between additional orbital symmetries and the observed geometric dependence. These reveal that d_{z^2} orbitals with spins pointing along either [001] or [110] can reproduce the reversed cross-section behavior with respect to $d_{x^2-y^2}$ orbitals. We also present there the case of d_{z^2} orbitals without a spin-flip process, i.e., involving only charge scattering. Although the agreement with the experimental data is better than for the case of $d_{x^2-y^2}$ orbitals, it is still worse than for the case of d_{z^2} orbitals with a spin-flip process. Furthermore, the calculations highlight that no configuration with in-plane $d_{x^2-y^2}$ orbitals comes close to reproducing the observed polarization- and angular-dependence of the Bragg peaks. Differentiating the possible spin scenarios, and whether there is mixed charge and spin character to the order, will require additional experimental input, such as a polarization analysis of the scattered X-rays that goes beyond the scope of the present work.

The present results therefore establish that the $x = 0.5$ NYN trilayer hosts a new kind of incommensurate Cu-based order that strongly involves the d_{z^2} orbitals and likely has a mixed spin/charge character. In the following, we denote it for simplicity as Cu- d_{z^2} order.

Resonant elastic X-ray scattering (REXS) study of the Bragg peak at $x = 0.5$

The Bragg peak of the $x = 0.5$ NYN trilayer due to the Cu density wave order at $Q_{\parallel} \approx -0.096$ r.l.u. and its unusual polarization dependence have also been observed with REXS experiments^{26,27}. In a REXS experiment the energy of the diffracted X-rays is not analyzed, the Bragg peak of the elastic signal is therefore superimposed on a background that includes the inelastic signal and thus is larger than in RIXS. The scattering geometry of the REXS experiment was adjusted to probe the Bragg peak in the same configuration as in the RIXS experiments, i.e., at $(HKL) = (-0.096, 0, 1.56)$. The value of H was scanned while keeping K and L constant by rotating the sample as well as the detector to vary the angle of incidence on the sample θ and the scattering angle 2θ . Note that $L = 1.56$ is close to the expected broad maximum of the Bragg-peak of the quasi-2D CDW order at $L = 1.5$, especially considering the finite size broadening of $\Delta Q_{\perp} = 0.053$ r.l.u. that arises from the small thickness of the YBCO layer of only 6 unit cells.

Figure 3 displays a wide-range H -scan at 9 K for both π and σ polarizations, which confirms that the Bragg peak due to the Cu- d_{z^2} order occurs on both sides of the specular peak at $(\pm 0.094, 0, 1.56)$. Moreover, it shows for both polarizations how the background has been accounted for with a polynomial function. Figure 3b displays the background subtracted response for both polarizations, which highlights a large difference between π and σ polarization in the intensity of the Bragg peaks that confirms the trend seen in the RIXS data evidencing a predominant d_{z^2} orbital

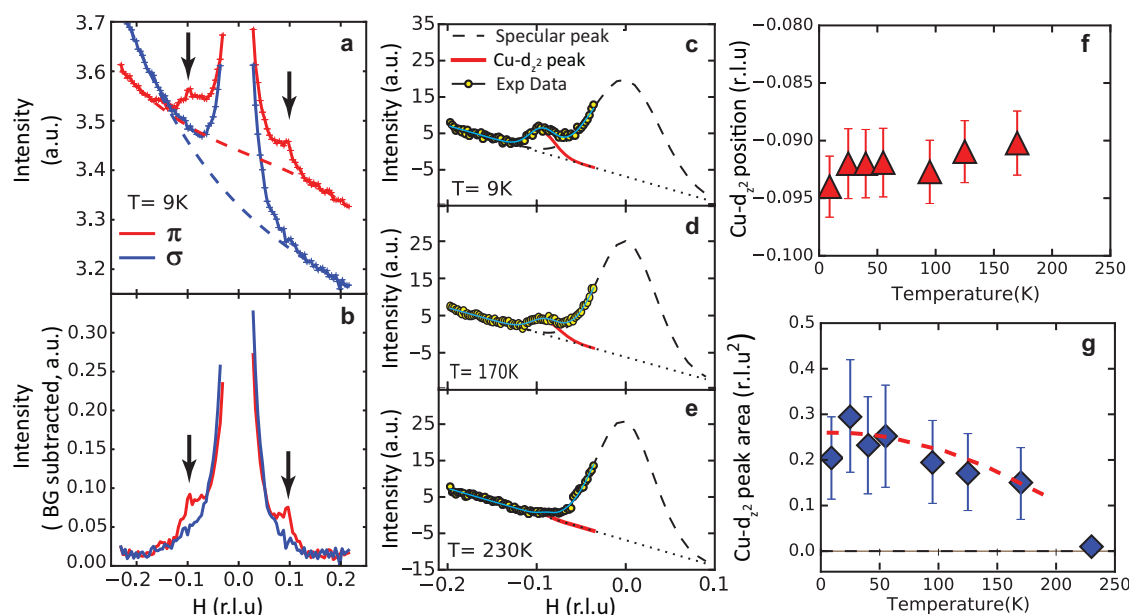


Fig. 3 Summary of a REXS study of the charge order peaks in a NYN trilayer with $x = 0.5$, $y = 0.25$. **a** Wide-range H -scan at 9 K which confirms that the Bragg peak due to the Cu- d_{z^2} order is seen on both sides of the specular peak. **b** Background subtracted scans showing the strong polarization dependence of the Bragg peaks due to the Cu d_{z^2} order that are marked by black arrows. **c–e** Partial scans of the Bragg peak around $(-0.096, 0, 1.56)$ for selected temperatures of 9, 170, and 230 K, respectively. For each temperature, the plotted experimental data (open circles) represent the average of several consecutively acquired scans. The solid cyan lines denote the total fit. The background (described with a linear function) is shown as dotted line and the specular peak (Gaussian function) with a dashed line. The obtained Bragg peak of the Cu d_{z^2} order is displayed by a solid red line. Graphs **(f)** and **(g)**, respectively, display the obtained temperature dependence of position and area of the Bragg peak of the Cu- d_{z^2} order. In graph **(g)**, the dashed red line is a guide to the eye. The propagation of uncertainty in peak position and area were calculated from the results of the fitting using standard procedures³⁹.

character of this Cu density wave order, as discussed in the previous section and shown in Fig. 2. Note that the width of the Bragg peak in the REXS data is larger than for the RIXS data in Fig. 1. We suspect that this difference is due to a lateral variation of the Bragg peak position and the larger beam spot for the REXS experiments ($H \times V$: $100 \mu\text{m} \times 50 \mu\text{m}$) as compared to RIXS ($H \times V$: $52 \mu\text{m} \times 4 \mu\text{m}$). Evidence for a variation of the Bragg-peak position in the range of $Q_{\parallel} = 0.09\text{--}0.1$ r.l.u. is indeed seen in the RIXS data, e.g., in Fig. 2 where the values differ between $-Q$ and $+Q$ and in the SOM (see Supplementary Fig. 6). Note that the RIXS data in the range of $\Delta E < 0.5$ eV do not show any inelastic component (see the intensity map in Fig. 1c) that might be peaked around $Q_{\parallel} \approx 0.09\text{--}0.1$ r.l.u. and thus might contribute to the peak seen in REXS.

Figure 3c–e displays representative curves of a temperature scan of the Bragg peak that was performed in π -polarization. The background has been described with a simpler, linear function that also provides a reasonable description of the background of the full scan around the specular peak (π -polarization, in Fig. 3a). Both the Bragg peak due to the charge order and the specular peak at $H = 0$ have been described with Gaussian functions. The temperature dependence of the obtained position and area of the Bragg peak is displayed in Fig. 3f, g. It reveals that the Bragg peak due to the static $\text{Cu-}d_{z^2}$ order persists to rather high temperature and vanishes well above 170 K. The $\text{Cu-}d_{z^2}$ order thus has a somewhat higher onset temperature than the Cu-CDW with $d_{x^2-y^2}$ character, which develops rather gradually below 150 K in bulk YBCO^{10,11} and in the range from 120 to 175 K in corresponding YBCO/manganite heterostructures with $x = 0.3\text{--}0.35$ ^{21,22}.

XAS and resonance of RIXS Bragg peak

We have complemented the above results with X-ray absorption spectroscopy (XAS) measurements that reveal important differences between the NYN trilayers for $x = 0.5$ and $x = 0.35$ with respect to the strength of the interfacial charge transfer and orbital reconstruction. Figure 4a shows a sketch of the XAS experiment with X-rays in π or σ polarization and an incidence angle of 30° . Information on the interfacial Cu ions and the bulk-like Cu ions is obtained from the comparison of the XAS spectra measured in total electron yield (TEY) and fluorescence yield (FY), respectively. Due to the small escape depth of the photo-excited electrons of only a few nanometers, the TEY signal arises predominantly from the Cu ions at the topmost YBCO/manganite interface. The FY signal, however, is equally sensitive to all Cu ions and thus representative of the majority of the Cu ions away from the interface.

Figure 4b, e compares the FY spectra of the trilayers with $x = 0.35$ and $x = 0.5$. These resemble the spectra of bulk-like YBCO showing a sharp resonance at 931 eV and a strong linear dichroism towards σ polarization (μ_{ab}) that confirms that the holes in the CuO_2 planes away from the interface have predominantly $d_{x^2-y^2}$ character. The corresponding TEY signal at $x = 0.35$ in Fig. 4c reveals some remarkable differences with respect to the FY signal. In particular, a clear redshift of the resonance by about 0.5 eV is observed, as well as a strong enhancement of the c -axis component μ_c with π -polarization that gives rise to a weak inversion of the X-ray linear dichroism (XLD). Both features were previously observed in YBCO/manganite multilayers with a similar hole doping of the manganite of $x = 0.3\text{--}0.35$ ²⁸. They have been explained in terms of a transfer of electrons from the manganite to the YBCO and an orbital reconstruction of the interfacial Cu ions that leads to a redistribution of holes from the $d_{x^2-y^2}$ to the d_{z^2} orbitals^{29,30}. Moreover, it has been shown that this charge transfer and orbital reconstruction are robust features that occur at this doping level irrespective of whether the manganite layer is an itinerant ferromagnetic^{29,30} or an AF charge/orbital ordered insulator²².

The more remarkable is our finding that for the TEY resonance of the trilayer with $x = 0.5$ in Fig. 4d both the red shift and the enhancement of the c -axis signal, and thus the interfacial charge transfer and orbital reconstruction are strongly reduced compared to the $x = 0.35$ sample in Fig. 4c. The reduced transfer of electrons from the manganite to the YBCO layer (or the smaller red shift of the TEY resonance) is naturally explained in terms of the larger hole doping of the manganite at $x = 0.5$, which lowers the Fermi-level of the manganite and thereby reduces its mismatch with respect to that of YBCO. The reason for the concomitant weakening of the orbital reconstruction of the interfacial Cu ions (i.e., a reduced density of d_{z^2} holes) is less obvious. It may involve additional effects such as a change of the position of the apical oxygen ion, which slightly reduces the hybridization of the d_{z^2} levels of the interfacial Mn and Cu ions. A full understanding requires further theoretical and experimental studies of the detailed structure of the interface, which hopefully will be motivated by our work.

Finally, Fig. 4f shows the evolution of the amplitude of the elastic Bragg peak in the RIXS data at $x = 0.5$ as a function of the incident photon energy (see Supplementary Note 5 and Supplementary Fig. 6 for more details and raw spectra). It exhibits a clear resonance with a maximum slightly below the resonance of the TEY-XAS signal (see Fig. 4d) and significantly below one of the resonance for the Bragg peak at $Q_{\parallel} \approx 0.3$ at $x = 0.35$ ²² and in plain YBCO³¹. This trend is consistent with our interpretation that this $\text{Cu-}d_{z^2}$ order originates predominantly from the interfacial CuO_2 planes. Certainly, it excludes the possibility that the $\text{Cu-}d_{z^2}$ originates from the CuO chains, for which the resonance would occur around 933.8 eV^{32,33}. Moreover, a Bragg-peak that arises from a superstructure of oxygen vacancies in the CuO chains would persist well above room temperature, in contrast to the trend shown in Fig. 3g.

DISCUSSION

The present work emphasizes the range of ordered phases that develop in the high- T_c cuprates, and, in particular, suggests that these can be induced to involve the out-of-plane orbitals, in contrast to previous observations. This raises important questions about the coupling mechanism at the cuprate/manganite interface that induces (or enhances) these different orders. It is likely that Jahn-Teller distortions due to the CE-type charge/orbital order of the manganite are induced that can be transported into the cuprate via the interfacial Ba-O layer. In turn, these distortions may trigger an orbital order of the interfacial CuO_2 layer through a variation of the orbital reconstruction along the interface with a certain alternation to the d_{z^2} and $d_{x^2-y^2}$ levels. A lateral ordering of the d_{z^2} and $d_{x^2-y^2}$ orbitals could also explain the magnetic component of the $\text{Cu-}d_{z^2}$ order that is suggested by our calculations. It would give rise to a modulation of the in-plane AF exchange couplings since the exchange between a pair of $d_{x^2-y^2}$ spins is strongly reduced when one orbital is replaced by a d_{z^2} orbital, and even becomes weakly ferromagnetic for spins on two adjacent d_{z^2} orbitals³⁰. Additionally, the $\text{Cu-}d_{z^2}$ order in the multilayer with $x = 0.5$ occurs despite a reduced density of d_{z^2} holes on the interfacial CuO_2 plane as compared to the multilayer with $x = 0.35$, for which the usual $d_{x^2-y^2}$ CDW order prevails. This suggests that an optimal density of d_{z^2} holes, or a particular ratio with respect to the $d_{x^2-y^2}$ holes, is required to stabilize the $\text{Cu-}d_{z^2}$ order and might be directly linked to its particularly long wavelength (small wave vector).

Another interesting aspect concerns the relationship of this Cu-based density wave order with superconductivity. The magneto-transport data of the NYN trilayer with $x = 0.5$ that are detailed in the (SOM) and reported in Khmaladze et al.²⁴ provide evidence for a strong granularity of the superconducting order. They also suggest that the grain boundaries, which break the

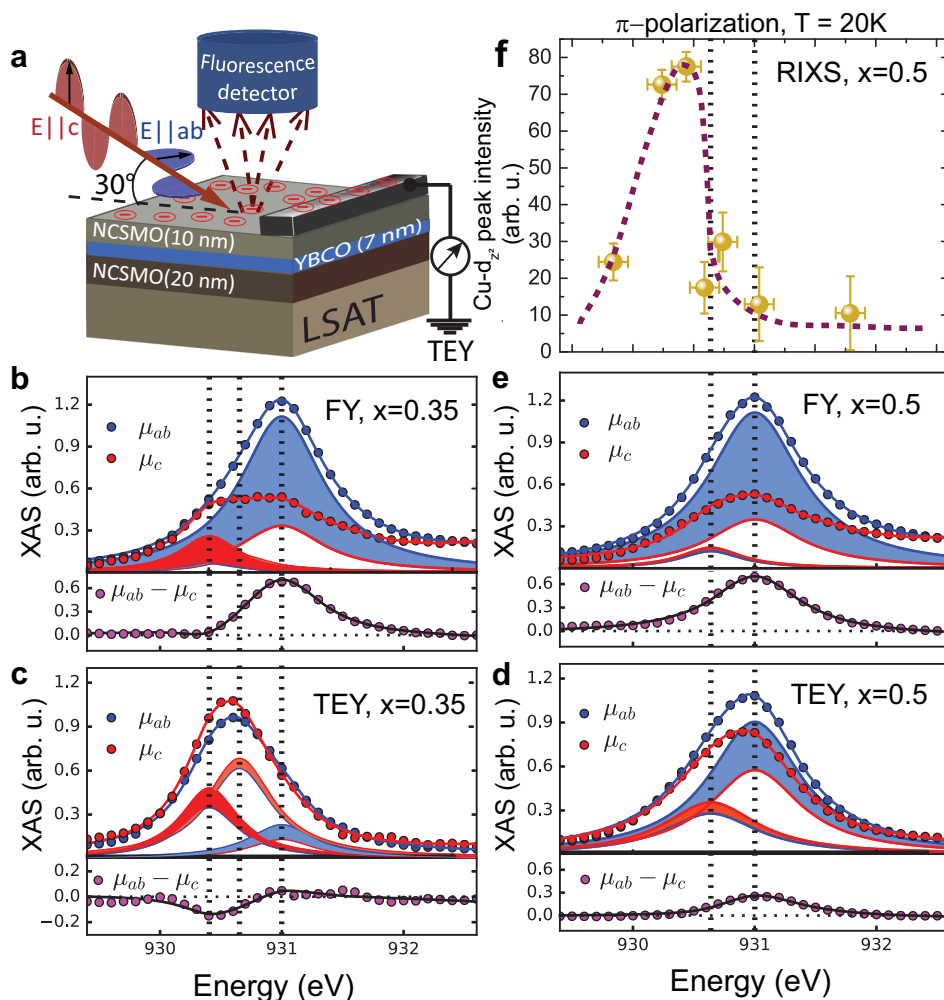


Fig. 4 Charge transfer and orbital reconstruction probed with XAS. **a** Schematic of the setup for measuring XAS in FY and TEY modes. **b–e** Comparison of the XAS spectra at the Cu L_3 -edge at 20 K and their X-ray linear dichroism (XLD) for NYN trilayers with $x = 0.35$ and $x = 0.5$. The FY spectra in **(b)** and **(e)** represent the response of all Cu ions whereas the TEY spectra in **(c)** and **(d)** are governed by the interfacial Cu ions. Solid symbols show the experimental data and solid lines are fitted Lorentzian functions. The peak at 931 eV arises from the bulk-like Cu ions whereas the peaks at 930.3 and 930.6 eV are attributed to the interfacial Cu ions. The redshift of the latter with respect to the bulk-like resonance is due to the transfer of electrons across the NCSMO/YBCO interface. The sign of the XLD of the peaks is shown by the colored shading: when $\mu_{ab} > \mu_c$ ($\mu_{ab} < \mu_c$) the difference is shaded blue (red). The spectra reveal that the charge transfer and the orbital reconstruction are considerably stronger at $x = 0.35$ than at $x = 0.5$. **f** Evolution of the intensity in π -polarization of the Bragg peak in the elastic RIXS signal at $Q_{||} \approx 0.096$ r.l.u. of the NYN trilayer with $x = 0.5$ as a function of the incident photon energy around the Cu L_3 -edge. It shows that the maximum occurs at a much lower energy than the one of the corresponding FY-XAS signal and even slightly below the one in the TEY-XAS (see panel **(e)**). The propagation of uncertainty were calculated from the results of the fitting using standard procedures (ref. ³⁹).

superconducting coherence and lead to Coulomb-blocking effects in the YBCO layer, are related to the domain boundaries of the Mn-CO in the manganite layers. Indeed, the Coulomb-blockade is stronger in NYN trilayers with $x = 0.35$, for which the Mn-CO order is weaker and more short-ranged (high density of domain boundaries), than in corresponding NYN trilayers with $x = 0.5$ (fewer domain boundaries)²⁴. Interestingly, the induced Cu-based density wave order follows a similar trend as the Mn-CO in that the correlation length of the $Q \approx -0.096$ r.l.u. order at $x = 0.5$ with $\xi \approx 40$ nm exceeds the one of the Cu-CDW with $Q \sim 0.3$ r.l.u. at $x = 0.35$ with $\xi < 10$ nm. This fits into the picture that the Mn-CO acts as a template for a Cu-based density wave order that is intertwined with the SC order with common domain boundaries at which the SC coherence is broken.

While many open questions remain, our findings open new routes for exploring the physics of intertwined ordered phases and demand both further theoretical and experimental work on the electronic and structural properties of the cuprate/manganite interface. They also

raise hopes that other exotic Cu-based orders can be induced by modifying the doping of the cuprate and manganite layers. In particular, the manganite provides a range of charge, orbital, and magnetic orders for which the interaction with the cuprate remains unexplored. Finally, with electric field gating it may even be possible to switch between different Cu-based orders at the YBCO/manganite interface to study their relationship with superconductivity or to develop new device and sensing applications.

METHODS

Sample growth and characterization

Trilayers of $\text{Nd}_{1-x}(\text{Ca}_{1-y}\text{Sr}_y)_x\text{MnO}_3(20 \text{ nm})/\text{YBa}_2\text{Cu}_3\text{O}_7(7 \text{ nm})/\text{Nd}_{1-x}(\text{Ca}_{1-y}\text{Sr}_y)_x\text{MnO}_3(10 \text{ nm})$ with $x = 0.5$, $y = 0.25$ and $x = 0.35$, $y = 0.2$ and a 1 nm thick LaAlO_3 capping layer were grown with pulsed laser deposition (PLD) on (001)-oriented $\text{La}_{0.3}\text{Sr}_{0.7}\text{Al}_{0.65}\text{Ta}_{0.35}\text{O}_3$ (LSAT) substrates. Details of the growth conditions and the sample characterization are given in Supplementary Note 1. The electronic transport and magnetization measurements showing the superconducting and magnetic properties of

the trilayers are reported in ref. 24. In particular, for the NYN trilayer with $x = 0.15$ and $y = 0.25$ the $R-T$ curve in zero magnetic field exhibits the onset of superconducting transition below $T_c \approx 82$ K followed by a steep increase of the resistance below about 60 K that is characteristic of a granular SC state. In 9 Tesla, a regular superconducting transition occurs with the same onset temperature that is completed below about 55 K. Note that the SC transition, which for fully oxygenated and thus slightly overdoped bulk YBCO is around 90 K, is typically reduced for very thin YBCO layers. In bare thin films this is due to finite size and strain effects as well as related defects. In addition, for the present multilayers, there is a reduction in the hole doping of the interfacial CuO_2 layers that arises due to the transfer of electrons from the neighboring manganite layers and the missing CuO chain layer at both the top and bottom interfaces^{30,34–36}.

Resonant inelastic X-ray scattering

The RIXS experiments at the $\text{Cu } L_3$ -edge were performed at the ADDRESS beamline of the Swiss Light Source (SLS) at the Paul Scherrer Institute (PSI) in Switzerland^{37,38}. The scattering angle between the incoming and outgoing X-ray beams was 130° . The angle δ , which gives the projection of transferred momentum along the surface direction, is defined as zero when the angles α and β are equal (specular reflection), i.e., $\delta = \Psi/2 - \alpha$. An energy resolution of 130 meV (full-width at half-maximum) was determined from the elastic scattering off a carbon-filled acrylic tape. The incident photon energy scale was shifted in order to match the X-ray absorption spectrum measured in TEY at ADDRESS beamline to the corresponding spectrum obtained at the XTreme beamline (see below). The energy scale of the incident energies used for the RIXS data has been corrected accordingly.

All the RIXS data presented in the main text are corrected for self-absorption assuming same light polarization for the incoming and outgoing beams. The correction procedure and the case of cross-polarization is discussed in Supplementary Note 3 of the SOM. The RIXS spectra used in Figs. 1 and 2 have been then normalized to the integrated intensity of the dd excitations.

RIXS cross-section calculations

Cross-section calculations for the RIXS process were performed using a single-ion model following Moretti Sala et al.²⁸. This calculation takes into account the atomic symmetries of the core-level p and valence d -orbitals and the geometry of the experimental setup, namely the π and σ polarization of incident light and the scattering angles of the experiment. Since measurements were performed at the $\text{Cu } L$ -edge, the atomic cross-sections of the elastic RIXS signal were calculated assuming X-ray absorption and emission to and from valence d -levels. We show here calculations for valence states with symmetry $d_{x^2-y^2}$ or d_{z^2} . Calculations for other d -orbitals have been performed, but are found not to correspond to the obtained data. (Supplementary Note 4). Processes without a spin-flip (elastic) and with spin-flip have both been calculated, assuming spin along the $[110]$ direction for $d_{x^2-y^2}$ states and along both $[001]$ and $[110]$ for d_{z^2} states. In order to compare the calculated cross-section with the observed RIXS intensities (arbitrary units), a constant conversion factor is applied, which is given in each of the figure captions.

Resonant elastic X-ray scattering (REXS)

REXS experiments at the $\text{Cu } L_3$ -edge (931 eV) were performed at the UE46 PGM-1 beamline of the BESSY II synchrotron at Helmholtz-Zentrum Berlin für Materialien und Energie (HZB) in Germany. The X-ray photodiode from the diffractometer can move in a continuous way to a large range of angles and the energy-integrating nature of the photodiode will show the elastic peak superimposed on a background that includes all the inelastic components. The scattering geometry of the REXS was adapted to probe the Bragg peak in similar configuration as RIXS experiments. The errors were calculated using ref. 39.

X-ray absorption spectroscopy

X-ray absorption spectroscopy (XAS) and X-ray linear dichroism (XLD) at the $\text{Cu } L_3$ -edge were measured in total electron yield (TEY) and fluorescence yield (FY) mode at the XTreme beamline of the SLS at the PSI in Switzerland.⁴⁰ The angle of incidence of the X-ray beam was set to 30° such that the response in σ polarization, μ_σ , corresponds to the ab plane response of YBCO, $\mu_{ab} = \mu_\sigma$, whereas the c -axis response, μ_c , is obtained from the signal in π -polarization, $\mu_\pi = \mu_c^*$ according to the geometrical factor, $\mu_c = 1/(\mu_\pi \cos^2(\theta) - \mu_\sigma \tan^2(\theta))$. In Fig. 3b–e the data have been

normalized to the maximum of the polarization-averaged absorption $\mu_{\text{avg}} = \max[(2\mu_{ab})/3]$ at the $\text{Cu } L_3$ -edge.

DATA AVAILABILITY

The data will be made available upon reasonable request to the corresponding authors.

Received: 30 July 2020; Accepted: 6 January 2021;

Published online: 10 February 2021

REFERENCES

- Keimer, B. et al. From quantum matter to high-temperature superconductivity in copper oxides. *Nature* **518**, 179–186 (2015).
- Alloul, H., Ohno, T. & Mendels, P. ^{89}Y NMR evidence for a fermi-liquid behavior in $\text{YBa}_2\text{Cu}_3\text{O}_{6+x}$. *Phys. Rev. Lett.* **63**, 1700–1703 (1989).
- Homes, C. C. et al. Optical conductivity of c axis oriented $\text{YBa}_2\text{Cu}_3\text{O}_{6.70}$: evidence for a pseudogap. *Phys. Rev. Lett.* **71**, 1645–1648 (1993).
- Lorama, J. W., Mirza, K. A., Cooper, J. R. & Tallon, J. L. Specific heat evidence on the normal state pseudogap. *J. Phys. Chem. Solids* **59**, 2091–2094 (1998).
- Niedermayer, C. et al. Common phase diagram for antiferromagnetism in $\text{La}_{2-x}\text{Sr}_x\text{CuO}_4$ and $\text{Y}_{1-x}\text{Ca}_x\text{Ba}_2\text{Cu}_3\text{O}_6$ as seen by muon spin rotation. *Phys. Rev. Lett.* **80**, 3843–3846 (1998).
- Julien, M. H. Magnetic order and superconductivity in $\text{La}_{2-x}\text{Sr}_x\text{CuO}_4$: a review. *Phys. B* **329–333**, 693–696 (2003).
- Tranquada, J. M. et al. Evidence for stripe correlations of spins and holes in copper oxide superconductors. *Nature* **375**, 561–563 (1995).
- Tranquada, J. M. et al. Coexistence and competition between, superconductivity and charge-stripe order in $\text{La}_{1.6-x}\text{Nd}_{0.4}\text{Sr}_x\text{CuO}_4$. *Phys. Rev. Lett.* **78**, 338–341 (1997).
- Wu, T. et al. Magnetic-field-induced charge-stripe order in the high-temperature superconductor $\text{YBa}_2\text{Cu}_3\text{O}_y$. *Nature* **477**, 191–194 (2011).
- Ghiringhelli, G. et al. Long-range incommensurate charge fluctuations in $(\text{Y,Nd})\text{Ba}_2\text{Cu}_3\text{O}_{6+x}$. *Science* **337**, 821–825 (2012).
- Chang, J. et al. Direct observation of competition between superconductivity and charge density wave order in $\text{YBa}_2\text{Cu}_3\text{O}_{6.67}$. *Nat. Phys.* **8**, 871–879 (2012).
- Fradkin, E., Kivelson, S. A. & Tranquada, J. M. Colloquium: theory of intertwined orders in high temperature superconductors. *Rev. Mod. Phys.* **87**, 457–482 (2015).
- Edkins, S. D. et al. Magnetic field-induced pair density wave state in the cuprate vortex halo. *Science* **364**, 976–980 (2019).
- Castellani, C., Castro, C. D. & Grilli, M. Singular quasiparticle scattering in the proximity of charge instabilities. *Phys. Rev. Lett.* **75**, 4650–4653 (1995).
- Caprara, S., Castro, C. D., Seibold, G. & Grilli, M. Dynamical charge density waves rule the phase diagram of cuprates. *Phys. Rev. B* **95**, 224511 (2017).
- Peng, Y. Y. et al. Re-entrant charge order in overdoped $(\text{Bi,Pb})_{2.12}\text{Sr}_{1.88}\text{CuO}_{6+\delta}$ outside the pseudogap regime. *Nat. Mater.* **17**, 697–702 (2018).
- Comin, R. et al. Charge order driven by Fermi-arc instability in $\text{Bi}_2\text{Sr}_{2-x}\text{La}_x\text{CuO}_{6+\delta}$. *Science* **343**, 390–392 (2014).
- Gerber, S. et al. Three-dimensional charge density wave order in $\text{YBa}_2\text{Cu}_3\text{O}_{6.67}$ at high magnetic fields. *Science* **350**, 949–952 (2015).
- Chang, J. et al. Magnetic field controlled charge density wave coupling in underdoped $\text{YBa}_2\text{Cu}_3\text{O}_{6+x}$. *Nat. Commun.* **7**, 11494 (2016).
- Kim, H. H. et al. Uniaxial pressure control of competing orders in a high-temperature superconductor. *Science* **362**, 1040–1044 (2018).
- Franco, A. et al. Long-range charge-density-wave proximity effect at cuprate/manganate interfaces. *Nat. Mater.* **15**, 831–834 (2016).
- Perret, E. et al. Coupled Cu and Mn charge and orbital orders in $\text{YBa}_2\text{Cu}_3\text{O}_7/\text{Nd}_{0.65}(\text{Ca}_{1-y}\text{Sr}_y)_{0.35}\text{MnO}_3$ multilayers. *Commun. Phys.* **1**, 45 (2018).
- Mallett, B. P. P. et al. Granular superconductivity and magnetic-field-driven recovery of macroscopic coherence in a cuprate/manganite multilayer. *Phys. Rev. B* **94**, 180503(R) (2016).
- Khmaladze, J. et al. Granular superconductivity and charge/orbital order in $\text{YBa}_2\text{Cu}_3\text{O}_7$ /manganite trilayers. *Phys. Rev. Mater.* **3**, 084801 (2019).
- Tokura, Y. Critical features of colossal magnetoresistive manganites. *Rep. Prog. Phys.* **69**, 797–851 (2006).
- Fink, J., Schierle, E., Weschke, E. & Geck, J. Resonant elastic soft x-ray scattering. *Rep. Prog. Phys.* **76**, 056502 (2013).
- Weschke, E. & Schierle, E. The UE46 PGM-1 beamline at BESSY II. *J. Large-scale Res. Facilities* **4**, A127 (2018).
- Moretti Sala, M. et al. Energy and symmetry of dd excitations in undoped layered cuprates measured by $\text{Cu } L_3$ resonant inelastic x-ray scattering. *New J. Phys.* **13**, 043026 (2011).
- Chakhalian, J. et al. Orbital reconstruction and covalent bonding at an oxide interface. *Science* **318**, 1114–1117 (2007).

30. Sen, K. et al. X-ray absorption study of the ferromagnetic Cu moment at the $\text{YBa}_2\text{Cu}_3\text{O}_7/\text{La}_{2/3}\text{Ca}_{1/3}\text{MnO}_3$ interface and variation of its exchange interaction with the Mn moment. *Phys. Rev. B* **93**, 205131 (2016).
31. Bluschke, M. et al. Stabilization of three-dimensional charge order in $\text{YBa}_2\text{Cu}_3\text{O}_{6+x}$ via epitaxial growth. *Nat. Commun.* **9**, 2978 (2018).
32. Achkar, A. J. et al. Distinct charge orders in the planes and chains of ortho-III-ordered $\text{YBa}_2\text{Cu}_3\text{O}_{6+6}$ superconductors identified by resonant elastic x-ray scattering. *Phys. Rev. Lett.* **109**, 167001 (2012).
33. Magnuson, M. et al. Self-doping processes between planes and chains in the metal-to-superconductor transition of $\text{YBa}_2\text{Cu}_3\text{O}_{6.9}$. *Sci. Rep.* **4**, 7017 (2014).
34. Malik, V. K. et al. Pulsed laser deposition growth of heteroepitaxial $\text{YBa}_2\text{Cu}_3\text{O}_7/\text{La}_{0.67}\text{Ca}_{0.33}\text{MnO}_3$ superlattices on NdGaO_3 and $\text{Sr}_{0.7}\text{La}_{0.3}\text{Al}_{0.65}\text{Ta}_{0.35}\text{O}_3$ substrates. *Phys. Rev. B* **85**, 054514 (2012).
35. Varela, M. et al. Nanoscale analysis of $\text{YBa}_2\text{Cu}_3\text{O}_{7-x}/\text{La}_{0.67}\text{Ca}_{0.33}\text{MnO}_3$ interfaces. *Solid-State Electron.* **47**, 2245–2248 (2003).
36. Salafraña, J. et al. Competition between covalent bonding and charge transfer at complex-oxide interfaces. *Phys. Rev. Lett.* **112**, 196802 (2014).
37. Ghiringhelli, G. et al. SAXES, a high resolution spectrometer for resonant X-ray emission in the 400–1600 eV energy range. *Rev. Sci. Instrum.* **77**, 113108 (2006).
38. Strocov, V. N. et al. High-resolution soft X-ray beamline ADDRESS at the Swiss light source for resonant inelastic X-ray scattering and angle-resolved photoelectron spectroscopies. *J. Synchrotron Radiat.* **17**, 631–643 (2010).
39. Bevington, P. R. *Data Reduction and Error Analysis for the Physical Sciences*, Ch. 4 and 5 (McGraw-Hill, New York, 1969).
40. Piamonteze, C. et al. X-Treme beamline at SLS: X-ray magnetic circular and linear dichroism at high field and low temperature. *J. Synchrotron Radiat.* **19**, 661–674 (2012).

ACKNOWLEDGEMENTS

We acknowledge fruitful discussion with Dr. Steven Johnston and experimental support provided by Dr. Enrico Schierle during the REXS beamtime. Work at the University of Fribourg was supported by the Swiss National Science Foundation (SNSF) through Grants No. 200020-172611 and CRSII2-154410/1. C.M. acknowledges the support by the SNSF grants No. PZ00P2_154867 and PP00P2_170597. The RIXS and XAS experiments were performed, respectively, at the ADDRESS beamline and the Xtreme beamline of the Swiss Light Source at the Paul Scherrer Institute. The work at the ADDRESS beamline is supported by the Swiss National Science Foundation through project no. 200021_178867, the NCCR MARVEL and the Sinergia network Mott Physics Beyond the Heisenberg Model (MPBH). The REXS experiments (Supplementary information) were performed at UE46_PGM-1 beamline at the BESSY II synchrotron in the Helmholtz-Zentrum, Berlin (HZB). This project received funding from the European Union's Horizon 2020 research and innovation program under grant agreement No. 730872. We thank J.-L. Andrey and O. Raetz from the Physics Department workshop at UniFr for technical assistance. T.C.A. acknowledges funding from the European Union's Horizon 2020 research and innovation programme under the Marie Skłodowska-Curie grant agreement No. 701647 (PSI-FELLOW-II-31 program).

AUTHOR CONTRIBUTIONS

RIXS measurements were carried out by R.G., C.W.N., M.R., S.S., E.P., Y.T., W.Z., T.C.A., T.S., C.M., and C.B. and analyzed by R.G. and C.W.N. Samples were grown and characterized by J.K. and S.S. Experimental support during the RIXS experiment, including alignment of the spectrometer and maintenance of the beamline were performed by E.P., Y.T., W.Z., D.M., T.C.A., and T.S.; XAS measurements were obtained by R.G. and C.P. and analyzed by R.G. The RIXS calculations were performed by C.W.N. and C.M. The REXS measurements were carried out by R.G., S.S., C.B., and E.W. and analyzed by R.G. and S.S. The manuscript was written by C.W.N., C.M., R.G., and C.B. with contributions from all authors. C.M. and C.B. were responsible for the overall project planning and direction. R.G. and C.W.N. have contributed equally.

COMPETING INTERESTS

The authors declare no competing interests.

ADDITIONAL INFORMATION

Supplementary information The online version contains supplementary material available at <https://doi.org/10.1038/s41535-021-00311-y>.

Correspondence and requests for materials should be addressed to R.G. or C.B.

Reprints and permission information is available at <http://www.nature.com/reprints>

Publisher's note Springer Nature remains neutral with regard to jurisdictional claims in published maps and institutional affiliations.



Open Access This article is licensed under a Creative Commons Attribution 4.0 International License, which permits use, sharing, adaptation, distribution and reproduction in any medium or format, as long as you give appropriate credit to the original author(s) and the source, provide a link to the Creative Commons license, and indicate if changes were made. The images or other third party material in this article are included in the article's Creative Commons license, unless indicated otherwise in a credit line to the material. If material is not included in the article's Creative Commons license and your intended use is not permitted by statutory regulation or exceeds the permitted use, you will need to obtain permission directly from the copyright holder. To view a copy of this license, visit <http://creativecommons.org/licenses/by/4.0/>.

© The Author(s) 2021, corrected publication 2021